ISSN 0016-7037
Volume 75, Number 1
January 1, 2011

Geochimica et Cosmochimica Acta

JOURNAL OF THE GEOCHEMICAL SOCIETY
AND THE METEORITICAL SOCIETY

Volume 75, Number 1 January 1, 2011

Articles

Continued on outside back cover

(This is a sample cover image for this issue. The actual cover is not yet available at this time.)

Available online at www.sciencedirect.com

SciVerse ScienceDirect

Geochimica et Cosmochimica Acta 75 (2011) 6870–6881

Geochimica et Cosmochimica Acta

www.elsevier.com/locate/gca

In situ atomic force microscopy measurements of biotite basal plane reactivity in the presence of oxalic acid

Simon J. Haward [a,b,c,*], Mark M. Smits [d,f], Kristín Vala Ragnarsdóttir [b,g], Jonathan R. Leake [d], Steven A. Banwart [e], Terence J. McMaster [a]

[a] H.H. Wills Physics Laboratory, University of Bristol, Bristol BS8 1TL, UK
[b] Department of Earth Sciences, University of Bristol, Wills Memorial Building, Queen's Road, Bristol BS8 1RJ, UK
[c] Department of Mechanical Engineering, Massachusetts Institute of Technology, 77 Massachusetts Avenue, Cambridge, MA 02139, USA
[d] Department of Animal and Plant Sciences, Alfred Denny Building, University of Sheffield, Western Bank, Sheffield S10 2TN, UK
[e] Department of Civil and Structural Engineering, Kroto Research Institute, North Campus, University of Sheffield, Broad Lane, Sheffield S3 7HQ, UK
[f] Centre for Environmental Sciences, Hasselt University, Agoralaan Building D, 3590 Diepenbeek, Belgium
[g] Institute of Earth Sciences, School of Engineering and Natural Sciences, University of Iceland, Askja, Sturlugata 7, Reykjavik 101, Iceland

Received 4 April 2011; accepted in revised form 6 September 2011

Abstract

We have used a direct imaging technique, in situ atomic force microscopy (AFM), to observe the dissolution of the basal biotite surface by oxalic acid over a range of temperatures close to ambient conditions, using a specially designed AFM liquid cell and non-invasive intermittent contact mode of operation. From the 3-dimensional nanometre-resolution data sets, we observe a process characterised by the slow formation of shallow etch pits in the (0 0 1) surface and fast growth of etch pits from the resulting steps, which represent proxies for the {h k 0} surface. Measurements of dissolution rates as a function of temperature allow a determination of an apparent activation energy ($E_{a,app}$) for the process, via mass-loss calculations from image analysis. We obtain a value of $E_{a,app} = 49 \pm 2$ kJ mol^{-1}, which is consistent with separate calculations based on planar area etch pit growth, and measurements of etch pit perimeters, indicating that this value of $E_{a,app}$ is representative of {h k 0} surface dissolution. The measurement of etch pit perimeters also enables an estimation of apparent activation energy as a function of step density indicating substantially higher apparent activation energy, up to $E_{a,app} = 140$ kJ mol^{-1}, on extrapolation towards a pristine surface with no defects. We suggest that this higher value of $E_{a,app}$ represents the slow formation of etch pits into the (0 0 1) surface.

1. INTRODUCTION

The weathering of primary silicate minerals plays a central role in the geochemical carbon cycle, in the formation of soil, and in the nutrition supply to plants in natural ecosystems. The global climate is regulated on multi-million year timescales by the balance of CO_2 supply to the atmosphere from volcanic and metamorphic degassing and the precipitation of carbonate minerals in marine environments by base cations (e.g. Ca and Mg) that increase the pH of water when released to solution through weathering of silicate rocks (Berner, 2004). Weathering of primary silicates leads to the formation of clay minerals, and iron and aluminium oxy(hydr)oxides, all of which play a vital role in soil structure and cation exchange capacity. Dissolution of silicates provides essential nutrient elements for

* Corresponding author at: Department of Mechanical Engineering, Massachusetts Institute of Technology, 77 Massachusetts Avenue, Cambridge, MA 02139, USA.
E-mail address: shaward@mit.edu (S.J. Haward).

0016-7037/$ - see front matter © 2011 Elsevier Ltd. All rights reserved.
doi:10.1016/j.gca.2011.09.010

plants, for example, biotite and hornblende are the primary sources of potassium (K^+) and magnesium (Mg^{2+}) in soil solution (Bowser and Jones, 2002).

Plants and their associated soil microbial populations are increasingly recognised as important drivers of silicate weathering, particularly through their effects in generating acidity and low molecular weight carboxylic acids which increase rates of hydrolysis of minerals (Banfield et al., 1999; Lucas, 2001). Plant roots and their associated symbiotic mycorrhizal fungi secrete large amounts of low molecular weight organic acids, up to 68 mmol L^{-1} of oxalic acid being found in soil solution in some coniferous forest soils (Griffiths et al., 1994).

Due to its importance, the dissolution of silicate minerals in the presence of organic acids has been studied by a wide variety of authors over several decades (Bennett and Casey, 1994; Hajash, 1994; Drever and Stillings, 1997; Oelkers and Schott, 1998; Stillings et al., 1998; van Hees et al., 2002; Cama and Ganor, 2006). These and other works have been summarised in an excellent recent review (Ganor et al., 2009). Organic acids may accelerate mineral dissolution via at least three principal mechanisms: (i) lowering the pH (i.e. increasing concentration of surface-adsorbed protons); (ii) the complexation of the organic ligand with metal cations on the mineral surface (Stumm and Furrer, 1987; Stumm and Wieland, 1990; Welch and Ullman, 1996; Cama and Ganor, 2006); and (iii) by forming aqueous complexes with Al or other metals that are directly involved in creating the rate controlling surface complex (Oelkers and Schott, 1998; Oelkers et al., 2008). For a given pH, the dissolution of a variety of minerals has been found to be significantly accelerated by an accompanying organic ligand, especially oxalate and citrate (Stumm and Wieland, 1990; Barman et al., 1992; Hamer et al., 2003; Golubev et al., 2006).

Biotite, a 2:1 tri-octahedral phyllosilicate containing K, Mg and Fe, is an abundant mineral that has been estimated to comprise about 8% of the exposed Earth's crust (Nesbitt and Young, 1984) being found especially in granitic rocks and low- to intermediate grade metamorphic rocks. Biotite can weather to form chlorite or vermiculite, resulting in the release of some of the cations, principally K^+, which is one of the three nutrients most in demand by plants (Eggleton and Banfield, 1985; Hinsinger and Jaillard, 1993). Biotite dissolution in organic and inorganic acids has been widely studied in laboratory reactors (Schnitzer and Kodama, 1976; Acker and Bricker, 1992; Barman et al., 1992; Kalinowski and Schweda, 1996; Malström and Banwart, 1997; Taylor et al., 2000; Murakami et al., 2003) and in the field (Murphy et al., 1998; Tu et al., 2007). Laboratory studies have been conducted under ambient temperature conditions over a range of pH from 0.5 to 10. Whilst these studies have reported incongruent dissolution of biotite, and provided some rate functions and mechanisms for this process, the activation energy for biotite dissolution has not been determined and the relative importance and mechanisms of organic and inorganic acid dissolution remain incomplete.

One complication in the study of biotite dissolution is that the sheet edges ({h k 0} surface) behave very differently from the surface of tetrahedral–octahedral–tetrahedral (TOT) layers ((0 0 1) surface) (Turpault and Trotignon, 1994). Leachate analysis from flow-through weathering reactors fails to distinguish which of the crystal faces have undergone alteration, and where secondary mineral phases are precipitated, the full extent of mineral alteration will be undetected in fluid chemistry. Atomic force microscopy (AFM) is a high resolution technique that enables the study of surfaces on a sub-nanometre level, yielding 3-dimensional data sets which may be used for quantitative measurement of process rates and energies alongside information on changes in surface topography at the atomic scale (Gratz et al., 1991; Lindgreen et al., 1991; Gratz et al., 1993; Jordan and Rammensee, 1996; Rufe and Hochella, 1999; Bosbach et al., 2000; Brandt et al., 2003; Aldushin et al., 2006).

In a study of particular relevance to the present work, Jordan and Rammensee (1996) used time-resolved sequences of AFM images to determine the dissolution rate at the step edge on a brucite (0 0 1) surface in "acidic water" (HCl, pH 2.7). By performing experiments over a range of temperatures (21–35 °C) they were able to use the Arrhenius relation to obtain a value for the apparent activation energy for the dissolution. Recently, similar in situ "hydrothermal" AFM methods have been applied to the study of apophylite and phlogopite dissolution in aqueous solutions over a pH range of 1.5–10 and temperatures between 20 and 140 °C (Aldushin et al., 2006). In acidic solutions at elevated temperature, etch pits were formed on the pristine phlogopite surface, which could accumulate in depth through many TOT layers. In contrast to the findings of Turpault and Trotignon (1994) with biotite, Aldushin et al. (2006) found that the dissolution of the basal and edge surfaces of phlogopite could occur at comparable rates at elevated temperatures. The results of Aldushin et al. (2006) also contrasted with the AFM imaging of chlorite dissolution in HCl (pH 2–5), in which dissolution proceeded by the growth of monolayer etch pits formed preferentially at defects in the basal surface (Brandt et al., 2003). To the best of our knowledge, no studies have been conducted to date that apply similar AFM imaging methods to the understanding of biotite dissolution processes and quantification of rates.

In this study we report the first real-time in situ observations of the response of the biotite (0 0 1) surface to HCl and oxalic acid solutions using AFM to quantify dissolution rates and to characterise the development of etch pits in the biotite surface. The relative effects of proton-promoted and ligand-promoted dissolution at the biotite (0 0 1) surface are investigated. The effects of temperature on the rates of oxalic acid dissolution of the biotite are determined using a novel system of temperature control, and an Arrhenius relationship for the dissolution rate of biotite is derived, enabling the apparent activation energy of the reaction to be calculated. The results provide important new insights into the rates and mechanisms of silicate weathering catalysed by oxalic acid, one of the most abundant low molecular-weight organic acids released into soil by plants and associated microorganisms.

2. MATERIAL AND METHODS

2.1. Sample description

The crystallo-chemical structure of biotite is illustrated in Fig. 1. A single TOT layer has a thickness of 1 nm and the negatively-charged layers (generated by the substitution of Al^{3+} for Si^{4+} into the tetrahedral layers) are bound together via K^{+} cations. Octahedrally coordinated magnesium and iron are sandwiched between the tetrahedral layers. The biotite sample (Krantz Company, Bonn, Germany), was mounted onto a sample holder and cleaved immediately prior to experimentation to expose a fresh (0 0 1) surface. The chemical composition of the biotite was determined with an electron probe microanalyser (Cameca S×100 Wavelength Dispersive EPMA), and the results are given in Table 1. The resulting chemical formula is: $K(Mg_{1.63}Fe_{1.37})[AlSi_3O_{10}](OH_{1.77}F_{0.23})$.

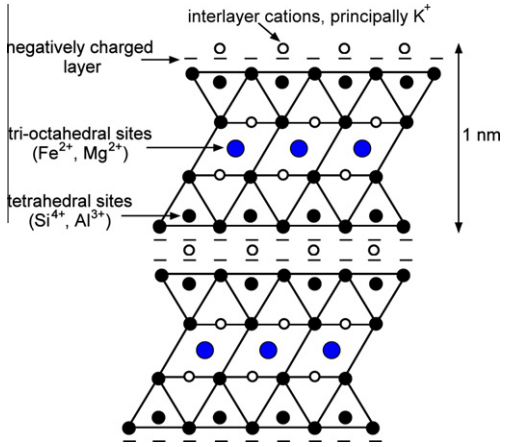

Fig. 1. Crystallo-chemical structure of biotite, showing the TOT layer thickness of 1 nm.

Table 1
Chemical composition of the biotite used in this study, determined by electron probe microanalysis.

Compound	Composition (%)
FeO	18.85
K_2O	9.38
MgO	12.57
CaO	0.07
Na_2O	0.06
Al_2O_3	13.46
P_2O_5	0.02
MnO	0.26
Cl	0.38
F	0.88
Cr_2O_3	0.01
TiO_2	2.37
SiO_2	37.17
Total	95.48

2.2. Atomic force microscopy

A digital instruments multimode AFM equipped with a NanoScope IIIA controller and extender module was used for this study. For experiments at room temperature a proprietary fluid cell was used. For experiments at reduced or elevated temperatures a modified fluid cell was constructed, which has been described in detail in a previous publication (Haward et al., 2011). Briefly, the modifications consisted of the insertion of a silicon rubber tube within the fluid cell, which made contact with the imaging liquid contained in the cell. A peristaltic pump (with a pulse dampener to eliminate vibration) was used to circulate either warm or cool water (maintained at constant temperature in a water bath) through the silicon rubber tube, thus heating or cooling the imaging environment. A bead thermistor was positioned within the fluid cell, close to the AFM probe, in order to monitor the temperature of the imaging fluid. By adjusting the rate of flow and the temperature of the heating/cooling water, it was possible to comfortably control the imaging temperature between $283\ K < T < 308\ K$, and maintain the temperature to within ± 0.5 K for the duration of an experiment.

Preliminary tests revealed that AFM in contact mode increased the dissolution susceptibility of the scanned surface. Fig. 2a shows the effect of scanning in contact mode; after scanning a small area repeatedly for around 1 h, when the scan area was enlarged a "scan box" became visible, where interactions with the AFM probe had worn away the mineral surface. Note that in AFM images height is indicated by a grey scale, with the highest points on the image appearing bright and the lowest points appearing dark. It is likely that in contact mode imaging the AFM probe abrades the sample, enhancing the dissolution rate in a manner similar to the effect observed for stirring on kaolinite dissolution (Metz and Ganor, 2001). However, using the less aggressive tapping mode imaging method on an atomically-flat biotite surface (biotite cleavage prior to imaging) exposed to oxalic acid, showed extremely low incidence of etch pit formation. Using tapping mode, the dissolution proceeded extremely slowly in the early stages causing extreme difficulties in maintaining stable imaging for sufficient time to observe the process. A pre-treatment of the surface to initiate pitting was employed, wherein a 100 μL aliquot of the particular acid solution of interest was applied to the freshly-cleaved biotite surface, and the AFM was engaged in contact mode using a 100 μm-long silicon nitride (SiN_4) cantilever (nominal spring constant 0.34 Nm^{-1}). A 5 × 5 μm area was scanned in this manner until a few etch pits in the surface became visible (usually after approximately 1 h, depending on the temperature). Subsequently, the AFM was disengaged, and the AFM was re-engaged using the same cantilever but this time in tapping mode. Following the re-engage in tapping mode, the scan area was zoomed-in to a 1.3 × 1.3 μm area and images were captured continuously at a scan rate of 2 Hz and resolution of 256 × 256 pixels, i.e. one image every 128 s. After a sufficient series of images had been captured the scan area was zoomed back to 5 × 5 μm to ensure that the interaction between probe and surface had not affected the rate of dissolution. Fig. 2b shows a 1.3 × 1.3 μm biotite surface after

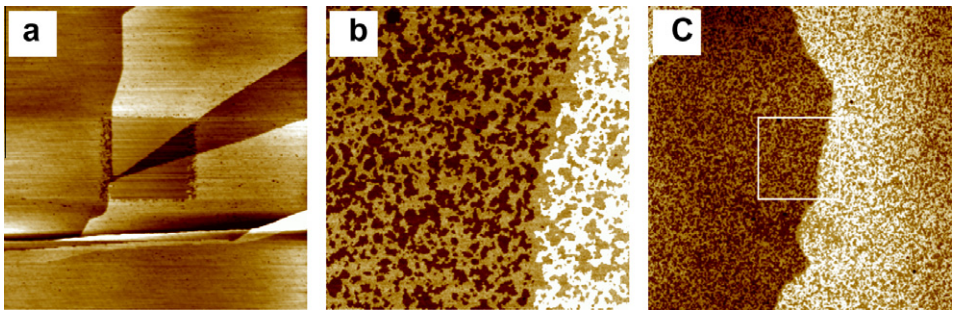

Fig. 2. (a) 5 × 5 μm image of a biotite surface in 15 mM oxalic acid showing the "scan-box" resulting from previous contact-mode imaging over a 1.3 × 1.3 μm area for approximately 1 h; (b) 1.3 × 1.3 μm image of a biotite surface in 100 mM oxalic acid that had been scanned in tapping mode for 90 min, after pre-treatment in contact mode to induce etch-pit formation; (c) 5 × 5 μm image of the same surface as image (b), showing no scan box. The original scan area is highlighted by the white square. Height in the images is represented by colour, with bright colours representing the highest points and dark colours representing the lowest. (For interpretation of the references to colour in this figure legend, the reader is referred to the web version of this article.)

90 min of scanning in tapping mode and Fig. 2c shows a subsequent 5 × 5 μm scan centred on the same area, which shows clearly that the AFM scanning has not affected the rate of biotite dissolution.

2.3. Solution composition

During the experiments it was not possible to follow the solution composition in the reactive solutions. Therefore the chemical affinity for the reactions is not known for either HCl or oxalate solutions. Table 2 gives the details for each experiment reported in this study, including temperature and pH.

2.4. Data analysis for quantification of dissolution rates and activation energy

Captured images were processed using proprietary image processing software (Veeco) and analysed using a bearing analysis routine to determine the percentage surface area occupied by etch pits. This percentage was then used to calculate the amount of dissolved biotite using the known thickness of a TOT layer ($z = 1 \times 10^{-9}$ m), the density ($\rho = 3090$ kg m^{-3}) and molecular weight ($MW = 0.4639$ kg mol^{-1}) of biotite, i.e.:

$$D = \frac{fz\rho}{MW}, \tag{1}$$

where D stands for biotite dissolved (in units of mol m^{-2}) and f is the fraction of the surface area covered by etch pits.

Table 2
Listing of experiments reported in this study.

Experiment no.	Acid	Concentration (M L^{-1})	pH	Temperature (°C)
1	Oxalic	0.01	2.09	28
2	Oxalic	0.1	1.32	28
3	Hydrochloric	0.1	1.26	28
4	Oxalic	0.1	1.32	10
5	Oxalic	0.1	1.32	19
6	Oxalic	0.1	1.32	35

A plot of dissolution as a function of time was obtained from each set of images at different temperatures, and dissolution rates were calculated from the linear portions of these rate functions, enabling an Arrhenius plot to be drawn according to the equation:

$$\ln(k) = \frac{-E_{a,app}}{R}\frac{1}{T}\ln(A), \tag{2}$$

where k is the dissolution rate (mol m^{-2} s^{-1}), T = temperature (K), A is the pre-exponential factor in the Arrhenius equation, and R is the ideal gas constant (8.314×10^{-3} kJ mol^{-1} K^{-1}). Since our measurements are of simple reaction rates, $E_{a,app}$ is an termed an 'apparent activation energy'. According to Eq. (2) the apparent activation energy is readily obtainable from the gradient of the Arrhenius plot of the logarithm of the dissolution rate as a function of the inverse temperature.

3. RESULTS AND DISCUSSION

3.1. Dissolution mechanism

Fig. 3 shows time sequences of tapping mode AFM images of biotite (0 0 1) surfaces in various acidic solutions at ambient temperature (301 K). Bright areas on the images are higher than dark areas, so the dark patches indicate holes in the TOT surfaces. Sequences (a) and (b) start at $t = 0$ min, defined as the time when the coverage of etch pits, formed by acid applied to the surface, is equal to approximately 10% of the surface in each case, and is the first AFM image taken on switching from contact to tapping mode. Subsequent images in the sequences are marked with the total passage of time since this first image was captured. Fig. 3A shows such a sequence covering 1 h in time for biotite in 0.01 M oxalic acid (pH = 2.09). The surface degradation is seen to proceed by a combination of etch pit formation and etch pit growth. Although the pre-treatment of the surface using contact mode accelerates the initiation of etch pit formation, new etch pits are also formed after the pre-treatment is finished and the imaging is done by tapping mode. Etch pits are found to have a depth of 1 nm, consistent with removal of a single complete TOT

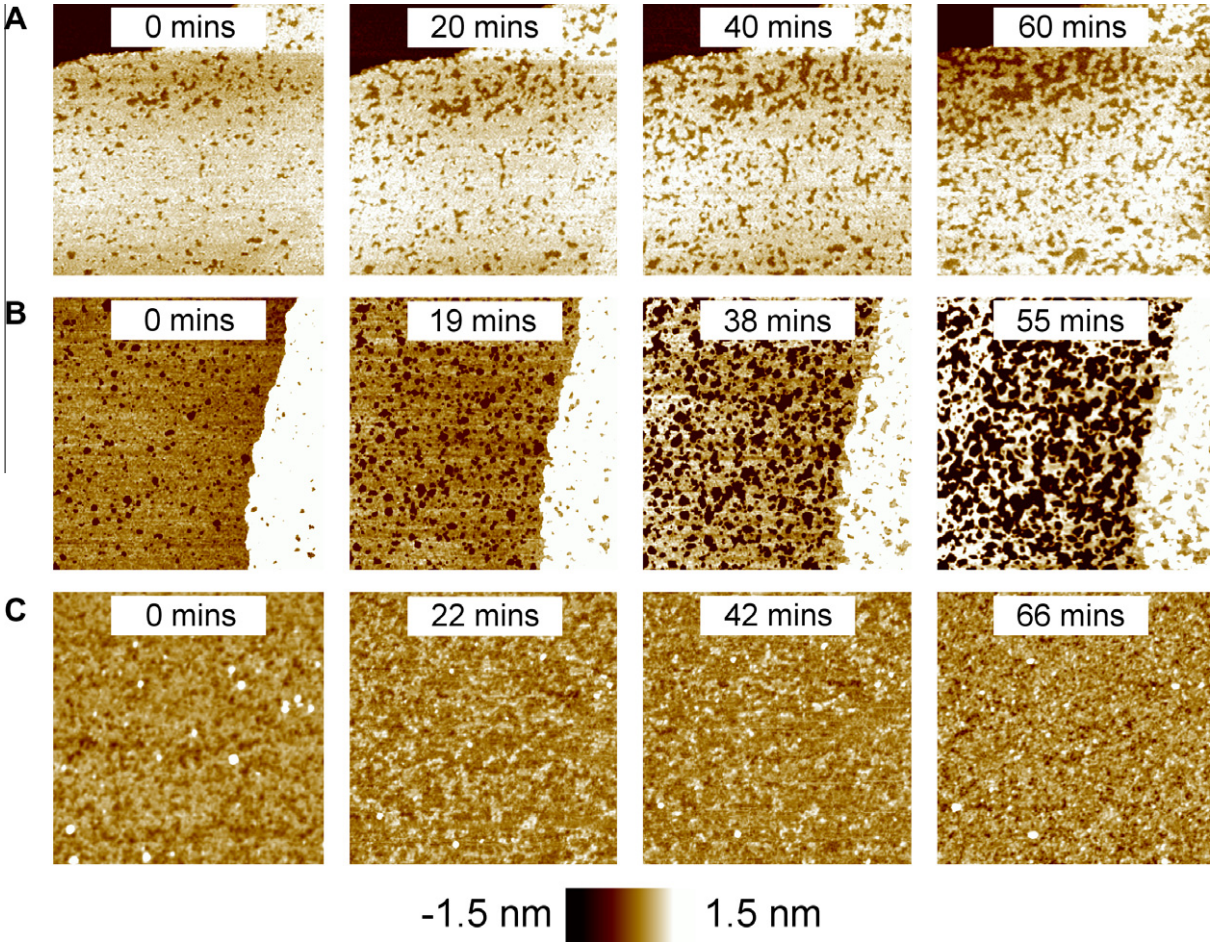

Fig. 3. Sequences of tapping-mode AFM images illustrating the dissolution of a biotite (001) surface in various acid conditions at $T = 301$ K: (A) 0.01 M oxalic acid; (B) 0.1 M oxalic acid; (C) 0.1 M HCl. All images are of 1.25 × 1.25 μm area, with z-range 3 nm as indicated by the scale bar.

layer. This is consistent with the depth of etch pits found in a muscovite (001) surface chemically weathered in the hyporheic zone of an Antarctic Dry Valley stream (Maurice et al., 2002). The loss of a complete TOT layer may result from leaching of the interlayer K^+, as suggested by Kalinowski and Schweda (1996). However, the apparent absence of remnants of undissolved tetrahedral or octahedral layers, which would likely remain on the surface and affect the AFM image, is more suggestive of complete dissolution of the entire TOT layer.

Dissolution of the entire TOT layer would suggest congruent dissolution of the biotite. Hamer et al. (2003) found an increasing tendency towards congruent dissolution as the pH decreased towards two for chlorite in various organic acids, and they found that oxalic acid increased dissolution rates by an order of magnitude compared to HCl and HNO_3 at 10 mM concentrations. At pH ~ 2 the congruent dissolution of the tetrahedral and octahedral layers of biotite (as opposed to transformation to a secondary mineral form) is also consistent with the findings of Acker and Bricker (1992), who investigated the dissolution of biotite over a pH range of 3–7, using dilute sulphuric acid. Incongruent dissolution of biotite in acidic solutions, as generally observed in bulk experiments in continuous flow-through reactors, may occur as a result of preferential leaching of certain cations from reactive sites at the edges of biotite sheets. Although the AFM imaging is restricted to the basal (001) surface of the biotite, as noted by Aldushin et al. (2006), the steps at the edges of etch pits represent a proxy for the {hk0} face.

It is apparent that once an etch pit has formed in the (001) surface the dissolution proceeds most rapidly along {hk0} direction as opposed to etching into the second TOT layer. This observation concurs with the work of Turpault and Trotignon (1994) who studied biotite dissolution in HNO_3 by varying the ratios of basal surface area to edge, or lateral, surface area of single crystal biotite samples. They found the sheet edges to be more reactive than the (001) surface and found a fast exchange of protons with the interlayer K^+. The general features of the dissolution process are reminiscent of the observations of Brandt et al. (2003) who observed etch pits of the depth of a single TOT layer (1 nm) and layer-by-layer dissolution of chlorite in a solution of pH 2 (HCl). However, our observations contrast with those of Aldushin et al. (2006) for the dissolution of phlogopite in acidic conditions (pH 1.5–2), who found that etch pits could extend up to 50 nm deep (50 TOT layers).

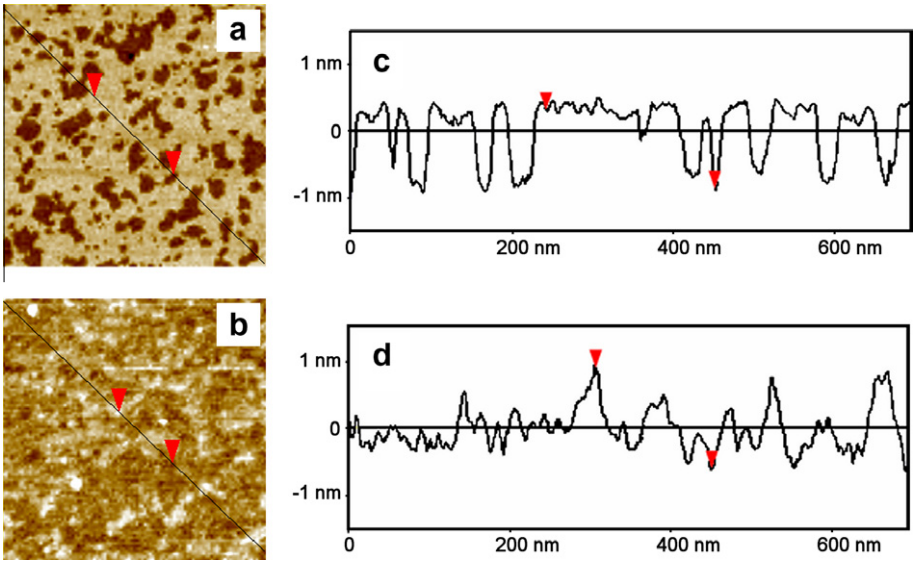

Fig. 4. Zoomed images of biotite surfaces after 40 min dissolution in: (a) 0.1 M oxalic acid; (b) 0.1 M HCl at $T = 301$ K. Panels (c) and (d) show line sections from (a) and (b), respectively.

The second sequence of images, Fig. 3B, is for biotite in a 0.1 M solution of oxalic acid (pH = 1.32, $T = 301$ K). The dissolution is seen to occur via similar processes of etch pit formation and growth observed in Fig. 3A, though clearly proceeds at a faster rate. The dissolution dynamics are reminiscent of a 2D Avrami process (Avrami, 1939), which can also be used to describe other nucleation and growth processes such as those of crystallization (Yip and Ward, 1996; Mahlin et al., 2004) and co-operative sequential adsorption (Abraham et al., 2000; Haward et al., 2010) in which nucleation is slow relative to growth.

The third series of images, Fig. 3C, is for biotite in 0.1 M HCl (pH = 1.26, $T = 301$ K). In this case the process of dissolution is visibly distinct from that shown in Fig. 3A and B. Rather than the formation and growth of discrete etch pits of 1 nm depth and the removal of a complete crystal layer, there is a widespread "roughening" of the biotite surface with numerous small indentations of varying depth, less distinct than the etch pits formed with oxalic acid. There are also numerous bright high spots on the surface, especially apparent at $t = 0$ min, which may be un-dissolved debris from the broken up mineral layer and would suggest incongruent dissolution in this case.

The depth of etch pits of ~1 nm is shown clearly by representative line sections across the biotite surface for both oxalic acid and hydrochloric acid dissolution, Fig. 4. Note that apparent roughness on the upper and lower surfaces of the line section in Fig. 4a and c (on the order of ±0.2 nm) is within the noise of the AFM instrument. That the formation of discrete etch pits is not observed in HCl, as was observed in dissolution by oxalate, is likely due to the lack of organic ligand to complex with surface metal cations. The roughening of the biotite surface in 0.1 M HCl shown by Figs. 3C and 4b and d is suggestive of the active exchange of potassium for protons, which was also reported in a previous AFM study on phlogopite surfaces in acidic conditions (Rufe and Hochella, 1999).

3.2. Rate calculation from (0 0 1) layer dissolution

The amount of biotite dissolved per metre squared of surface as a function of time is shown for each of the oxalic acid solutions (Fig. 5) and is derived from the images in Fig. 3A and B using Eq. (1). We observe initially slow dissolution where etch pits are few and small, and as the etch pits expand, and more are formed, the dissolution rate gradually increases, which is due to the increase in reactive {h k 0} surface area resulting from the increase in the number and size of etch pits.

The effect of temperature (283 K < T < 308 K) on biotite dissolution in 0.1 M oxalic acid is shown in the time-course sequence of images in Fig. 6A–D. As before, the first image ($t = 0$) in each sequence represents a starting point for the dissolution process where etch pits cover approximately 10% of the surface in each case. Note that in these AFM images the colour representing the $z = 0$ nm plane is constant but its position can 'float' in a manner depending on the proportion of surface found above and below

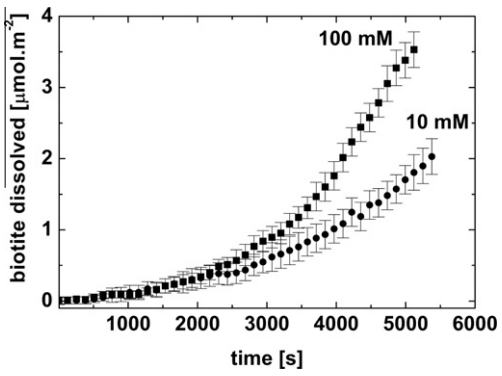

Fig. 5. Amount of dissolved biotite as a function of time in 0.1 and 0.01 M oxalic acid solutions at $T = 301$ K.

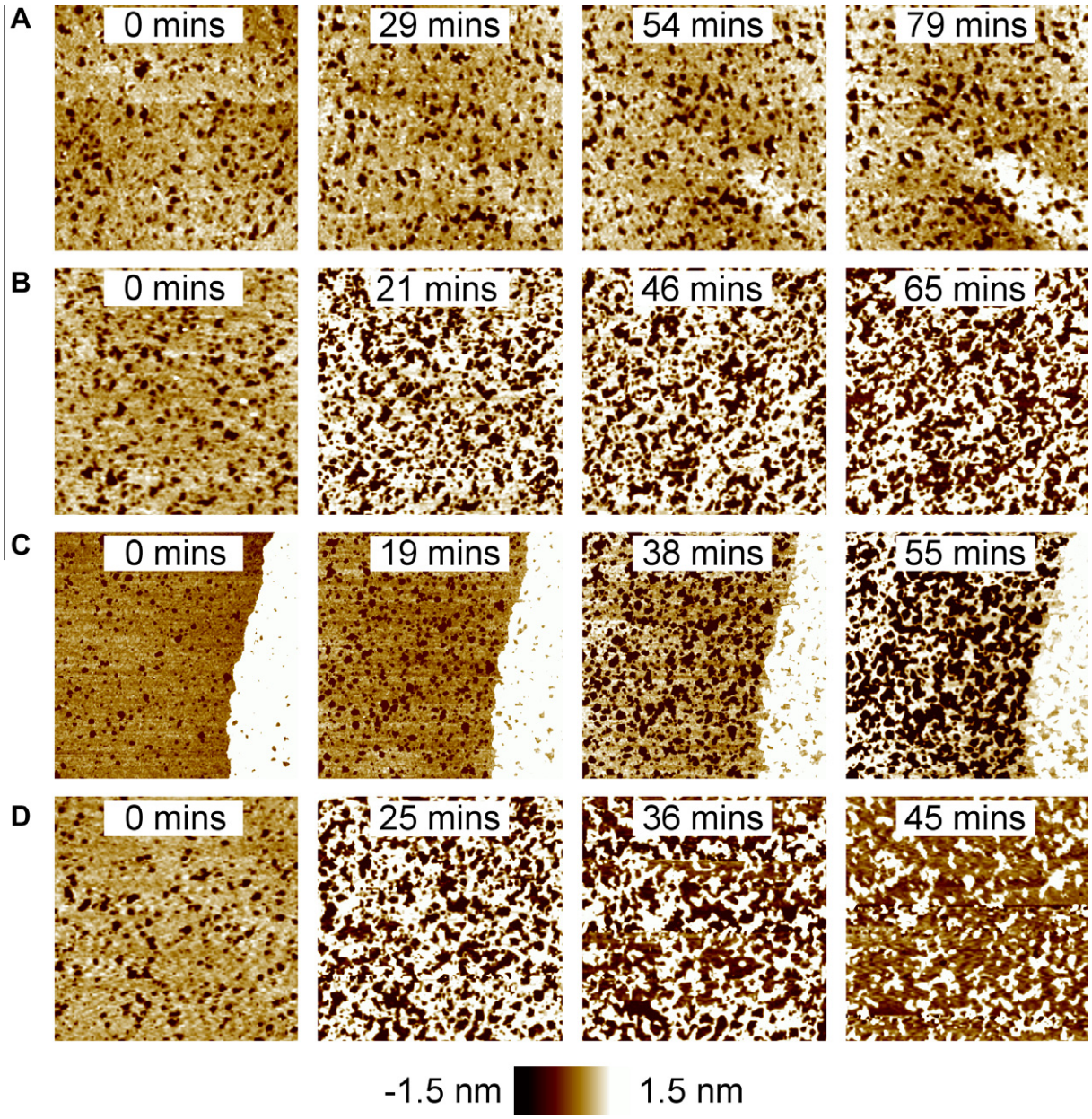

Fig. 6. Sequences of tapping-mode AFM images depicting the dissolution of a biotite (0 0 1) surface in 0.1 M oxalic acid at various temperatures: (A) $T = 283$ K; (B) $T = 292$ K; (C) $T = 301$ K; (D) $T = 308$ K. All images are of 1.25×1.25 μm area, with z-range 3 nm as indicated by the scale bar.

$z = 0$ nm. Hence, as etch pits expand to cover more of the surface the position of the $z = 0$ nm plane shifts from the upper (0 0 1) layer towards the lower (0 0 1) layer and the image evolves from the appearance of an upper layer containing dark holes to a lower layer punctuated by bright plateaus (observe for example the evolution in appearance of Fig. 6D over time). It is very clear that the biotite surface dissolves more rapidly as the temperature is increased, but, qualitatively, the process of etch pit formation and growth appears similar at all temperatures.

Analysis of the images in Fig. 6, along with the remainder of the images in each data set, provides the dissolution curves shown in Fig. 7a. The curves obtained at each experimental temperature all show qualitative similarities: slow dissolution associated with the initial formation of etch pits (the formation of surface complexes) and a gradually increasing dissolution rate as etch pits grow and access of acid to metals in TOT sites increases (detachment of the surface complexes). As oxalate–metal complexes are released into the solution, more oxalate can adsorb to the freshly exposed surfaces and the dissolution process thus proceeds. The dissolution rate reaches a constant value, indicated in each case by the solid grey line, which tends to start when etch pits cover approximately 20% of the surface (this corresponds to 1.5×10^{-6} mol m^{-2} biotite dissolved). The analysis is terminated at approximately 50%

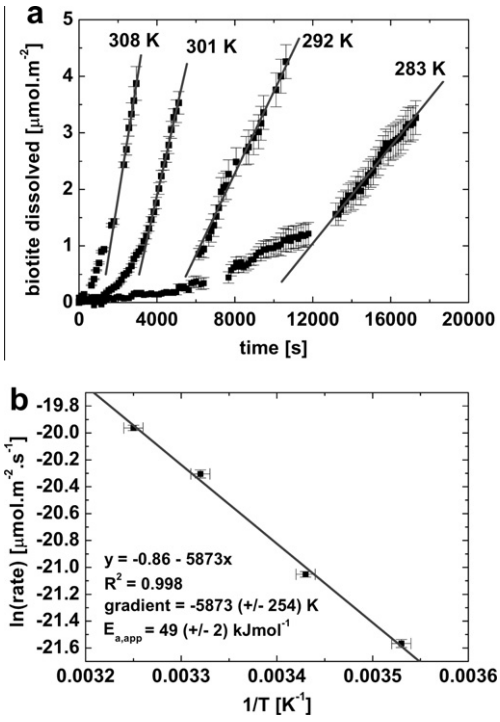

Fig. 7. (a) Amount of dissolved biotite as a function of time in 0.1 M oxalic acid at the temperatures indicated. Gaps in the plots arise where AFM images were not of sufficient quality for accurate analysis of etch-pit coverage. Solid grey lines fit to the portions of the curves over which the dissolution is approximately linear ($R^2 > 0.99$) with time, and used to calculate the dissolution rate constant for the Arrhenius equation. The dissolution rates determined from the gradients of the fitted lines are: 0.00043 µmol m^{-2} s^{-1} ($T = 283$ K), 0.00072 µmol m^{-2} s^{-1} ($T = 292$ K), 0.0015 µmol m^{-2} s^{-1} ($T = 301$ K), 0.0021 µmol m^{-2} s^{-1} ($T = 308$ K); (b) Arrhenius plot for biotite dissolution in 0.1 M oxalic acid, showing the apparent activation energy, $E_{a,app} = 49 \pm 2$ kJ mol^{-1}.

etch pit coverage (4×10^{-6} mol m^{-2} dissolved biotite) due to the subsequent ligand promoted dissolution into the next underlying TOT layer (data not shown). The more irregular nature of the biotite surface as it is dissolved by HCl (Fig. 3), specifically the lack of a well-defined basal plane as in the case of oxalic acid dissolution, means that explicit quantification of the loss of material is not possible.

Although the curves in Fig. 7a are almost parabolic at low times, they tend to linearity at higher times. Lines of best fit have been fitted to the curves over regions where the R^2 value for linearity exceeds 0.99. The gradients of the linear portions of the dissolution curves are taken to be the steady values of the dissolution rate, k, used for the determination of the apparent activation energy, $E_{a,app}$, according to Eq. (2). The values of k are: 4.3×10^{-10} mol m^{-2} s^{-1} at 283 K; 7.5×10^{-10} mol m^{-2} s^{-1} at 292 K; 1.5×10^{-9} mol m^{-2} s^{-1} at 301 K and 2.1×10^{-9} mol m^{-2} s^{-1} at 308 K. These values lie at the lower end of the range of dissolution rates considered observable by in situ AFM (Dove and Platt, 1996). At close to room temperature (i.e. at 292 K) the dissolution rate that we measure is considerably faster than that reported by Kalinowski and Schweda (1996) for biotite at similar pH ($\sim 10^{-10}$ mol m^{-2} s^{-1}); this is likely due to their use of simple acids (HCl and H_2SO_4) and hence absence of organic metal-complexing ligand. Unfortunately our AFM experiments did not allow extraction of dissolution rates for biotite in HCl so we can not make a more exact comparison. The rate that we report for biotite dissolution in 0.1 M oxalic acid at room temperature is very comparable to that reported in the AFM study by Rufe and Hochella (1999) for the dissolution of the {h k 0} surface of phlogopite ($\sim 3 \times 10^{-10}$ mol m^{-2} s^{-1}), but orders of magnitude higher than the rate they reported for total average dissolution rate ($\sim 3 \times 10^{-12}$ mol m^{-2} s^{-1}). Our dissolution rate with temperature is also approximately an order of magnitude higher than the rate reported by Aldushin et al. (2006) for the dissolution of the {h k 0} surface and nearly three orders of magnitude higher than the rate reported for the (0 0 1) surface of phlogopite in HNO_3.

The Arrhenius plot resulting from the values of dissolution rate (Fig. 7a) is presented in Fig. 7b, and yields an apparent activation energy for biotite dissolution in oxalic acid of $E_{a,app} = 49 \pm 2$ kJ mol^{-1}, where the error is determined from the error in gradient of the straight-line fit to the data. Since etch pit growth proceeds much faster than etch pit nucleation, our measured value of $E_{a,app}$ probably best corresponds to that for dissolution of an {h k 0} surface. Our value is comparable to that of $E_{a,app} = 60 \pm 12$ kJ mol^{-1} determined by Jordan and Rammensee (1996) for brucite dissolution in acidic water (HCl) and also lies within the range of 30–60 kJ mol^{-1} found for the release of various elements from granitoid rocks (White et al., 1999).

The data of Fig. 7a can be used to estimate the time required for the dissolution of a complete TOT layer in each situation (assuming the entire layer is in contact with the acid). A single TOT layer of thickness 1 nm and area 1 m^2 has a mass of $\sim 3 \times 10^{-6}$ kg, which is equivalent to ~ 7 µmol of biotite. The curves in Fig. 7a can be extrapolated using the lines of best fit to find the time at which 7 µmol m^{-2} has dissolved. In 0.1 M oxalic acid at room temperature the time required is approximately 2 h per layer.

3.3. Measurement of average etch pit growth

At all temperatures a linear relationship was found between the dissolution of the biotite layer with time squared, as shown in Fig. 8a. Assuming the rate of etch pit formation is low compared with the rate of growth (as we observe), this is indicative of the dimension of the average etch pit growing linearly with time, i.e. for a circular etch pit the radius would grow linearly with time. Hence, by taking the square-root of the gradient of each line shown in Fig. 8a, we can obtain values proportional to the rate of retreat of the etch pit edge for each temperature; plotting these to an Arrhenius equation (Fig. 8b) yields a value for the apparent activation energy of $E_{a,app} = 53 \pm 3$ kJ mol^{-1} (where the error is again determined from the error in gradient of the straight-line fit to the data).which is consistent with our mass-loss calculation.

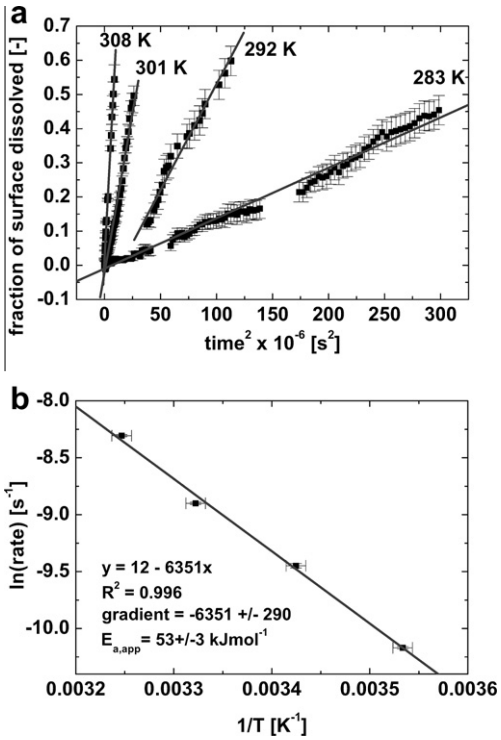

Fig. 8. (a) Fraction of biotite surface dissolved as a function of time squared, at the temperatures indicated. Solid grey lines indicate linear lines of best fit. The gradients of the fitted lines in (a) are: $1.47 \times 10^{-9}\ s^{-2}$ ($T = 283$ K), $6.21 \times 10^{-9}\ s^{-2}$ ($T = 292$ K), $18.6 \times 10^{-9}\ s^{-2}$ ($T = 301$ K), $61.0 \times 10^{-9}\ s^{-2}$ ($T = 308$ K); (b) the square root of the gradients from panel a are taken as the dissolution rate and used to find the apparent activation energy.

3.4. Calculation of individual etch pit growth

Analysis of the planar growth of individual etch pits was also performed. Thirty separate etch pits were followed over time for each temperature, and the average diameter of each etch pit was measured using image analysis software (Image Pro Plus, MediaCybernetics), showing a linear increase in diameter with time, as expected. A linear regression was applied to each etch pit, and average etch pit diameter increase was calculated at various temperatures. Fig. 9 shows the Arrhenius plot arising from these measurements and yields an apparent activation energy of $E_{a,app} = 51 \pm 9$ kJ mol^{-1}. This analysis of a number of individual etch pits complements the treatment shown in Fig. 8, which is based on the average rate of growth of all the etch pits in the scan area. Etch pit growth clearly corresponds to dissolution at step edges, or at {h k 0} surfaces.

3.5. Evolution of step edges and calculation of activation energy as a function of step-density

The correlation between the biotite dissolution rate and the density of step-edges was also investigated. The dissolution rate was calculated by examining the difference in surface area loss between pairs of consecutive images and dividing by the time interval between the pair of images.

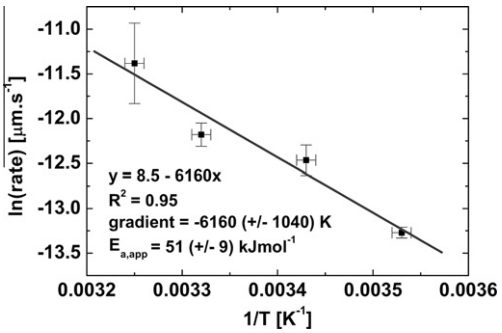

Fig. 9. Arrhenius plot obtained by direct measurement of etch pit diameter as a function of time.

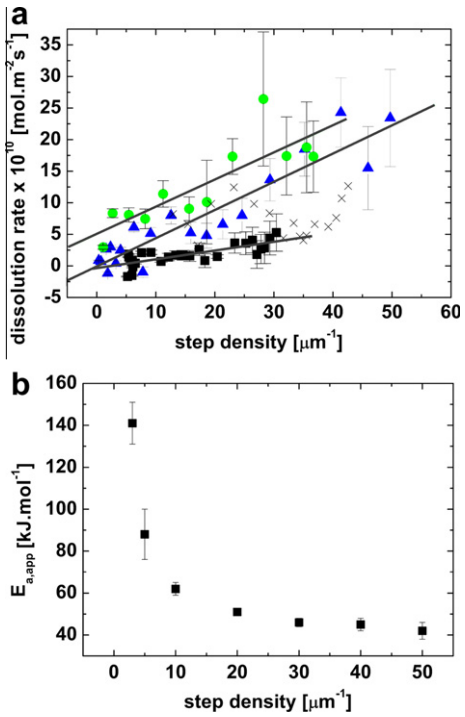

Fig. 10. (a) Dissolution rate as a function of step density for biotite in 0.1 M oxalic acid at $T = 283$ K (black squares), $T = 292$ K (black crosses), $T = 301$ K (blue triangles), $T = 308$ K (green circles). The grey lines of best fit to the data have equations: $y = -0.37 + 0.14x$, $R^2 = 0.61$ (283 K), $y = -0.06 + 0.45x$, $R^2 = 0.86$ (301 K), $y = 5.1 + 0.43x$, $R^2 = 0.71$ (308 K); (b) apparent activation energy as a function of step density, derived from panel 10a. (For interpretation of the references to colour in this figure legend, the reader is referred to the web version of this article.)

The step density was determined by measuring and summing the perimeter lengths of all the etch pits in each image and dividing by the scan area. Linear relationships between dissolution rate and step density were observed at three of the four experimental temperatures, see Fig. 10a. The exception was at 292 K, when no clear correlation was found. We believe the few negative values of dissolution rate recorded at low step density at 283 K and 301 K are

simply scatter as a result of occasional noisy AFM scans; we do not think there is any genuine growth of the surface. The straight lines-of-best-fit on Fig. 10a can be extrapolated to a step density of zero. At $T = 283$ and 301 K the lines-of-best-fit pass very close to the origin of coordinates (y-intercepts of $(-0.4 \pm 0.4) \times 10^{-10}$ mol m^{-2} s^{-1} and $(0 \pm 1) \times 10^{-10}$ mol m^{-2} s^{-1}, respectively). This indicates that at these lower temperatures the dissolution process is dominated by dissolution of the sheet edges (i.e. lateral growth of etch pits) as opposed to formation of etch pits in the (0 0 1) surface. However, at 308 K, the line-of-best-fit passes significantly above the origin (y-intercept $= (5 \pm 2) \times 10^{-10}$ mol m^{-2} s^{-1}), indicating that at this temperature dissolution could proceed slowly even into a pristine (0 0 1) surface. Of course, even a freshly cleaved biotite "pristine" surface may include defects/very small pits from which dissolution could proceed into the {h k 0} surface. However, despite the scatter and noise in this data, it certainly appears there is a shift in behaviour at the highest temperature. It may be that we are, like other researchers (Oelkers et al., 2008) observing a key temperature threshold that (via activation energy) results in minerals undergoing a step-change in weathering.

Ignoring the data obtained at 292 K, Fig. 10a can be used to investigate further the apparent activation energy by finding the dissolution rate as a function of temperature for a given value of step density and applying the Arrhenius equation again. However, the apparent activation energy varies depending on the choice of step density, see Fig. 10b. At very low step densities high values of up to $E_{a,app} = 140$ kJ mol^{-1} are found for the apparent activation energy. This value decreases monotonically with increasing step density and finally settles to a value of around $E_{a,app} = 40$ kJ mol^{-1} when the step density exceeds $\sim$30 μm^{-1}. It is tempting to explain this change in terms of a separation of two distinct processes involved in the dissolution: etch pit formation and etch pit growth. Etch pit formation into the (0 0 1) basal surface is slow and requires a high apparent activation energy; on the other hand etch pit growth into the {h k 0} surface is faster and results in a lower apparent activation energy.

4. CONCLUSIONS

We have used in situ real-time AFM imaging to provide visual information on the process of dissolution of the biotite (0 0 1) surface in 0.01 and 0.1 M oxalic acid and 0.1 M hydrochloric acid. For oxalic acid at both concentrations at room temperature we observe a process of slow formation of etch pits in the biotite surface followed by relatively fast expansion of the etch pits over the surface. Analysis of etch pit coverage as a function of time allows straightforward assessment of the dissolution rate. Experiments performed over a range of temperatures in 0.1 M oxalic acid have thus allowed us to use the Arrhenius equation to determine a value for the apparent activation energy of $E_{a,app} \approx 50$ kJ mol^{-1} for the dissolution. However, our work indicates significantly higher values for $E_{a,app}$ (up to $\sim$140 kJ mol^{-1}) when the density of step-edges on the surface is low. This is also consistent with visual observations of the relative rates of etch pit formation and growth.

In the absence of oxalate (i.e. in HCl solution) formation of discrete etch pits is not observed, most likely due to the lack of organic ligand to complex with Al^{3+}. As a result, while interlayer and octahedral cations are still gradually leached, the silica skeleton could remain relatively intact resulting in what may be incongruent dissolution and the observed rough and perhaps amorphous surface structure.

The emerging mechanism of the dissolution process of the (0 0 1) biotite surface in oxalic acid is of initial etch pit formation in the surface due to surface ligand complexation of tetrahedral (Al^{3+}) and octahedral (Mg^{2+}, Fe^{2+}) cations. This exposes the {h k 0} crystal surface to attack, resulting in depletion of interlayer K^+ cations by displacement with H^+ and increasing the number of available sites for oxalate complexation with both octahedral and tetrahedral ions. This results in rapid growth of the etch pit, relative to the rate of etch pit formation in the pristine (0 0 1) surface. We therefore suggest that the processes that initiate pitting or loss of the top of the TOT layer are the rate-limiting steps in dissolution of biotite.

Our intention for the future is to apply our AFM imaging methods to the study of phyllosilicate dissolution in organic acids at concentrations of environmental relevance. This will give valuable insight into the biota-induced weathering mechanisms that are the ultimate motivation for this course of work.

ACKNOWLEDGEMENTS

This study was funded by the Natural Environment Research Council (NERC) Consortium Grant No. NE/C521044/1 and the Worldwide Universities Network. We are indebted to our colleagues in the Weathering Systems Consortium at the Universities of Sheffield, Leeds and Bristol for insightful discussions.

REFERENCES

Abraham T., Giasson S., Gohy J. F., Jerome R., Muller B. and Stamm M. (2000) Adsorption kinetics of a hydrophilic–hydrophobic diblock polyelectrolyte at the solid-aqueous solution interface: a slow birth and fast growth process. *Macromolecules* **33**, 6051–6059.

Acker J. G. and Bricker O. P. (1992) The influence of pH on biotite dissolution and alteration kinetics at low temperature. *Geochim. Cosmochim. Acta* **56**, 3073–3092.

Aldushin K., Jordan G. and Schmahl W. W. (2006) Basal plane reactivity of phyllosilicates studied in situ by hydrothermal atomic force microscopy (HAFM). *Geochim. Cosmochim. Acta* **70**, 4380–4391.

Avrami M. J. (1939) Kinetics of phase change I: general theory. *J. Chem. Phys.* **7**, 1103–1112.

Banfield J. F., Barker W. W., Welch S. A. and Taunton A. (1999) Biological impact on mineral dissolution: application of the lichen model to understanding mineral weathering in the rhizosphere. *Proc. Natl Acad. Sci. USA* **96**, 3404–3411.

Barman A. K., Varadachari C. and Ghosh K. (1992) Weathering of silicate minerals by organic acids. I. Nature of cation solubilisation. *Geoderma* **53**, 45–63.

Bennett P. C. and Casey W. (1994) Chemistry and mechanisms of low temperature dissolution of silicates by organic acids. In *Organic Acids in Geological Processes* (eds. E. D. Pittman and M. D. Lewan). Springer-Verlag, Berlin.

Berner R. A. (2004) A model for calcium, magnesium and sulfate in seawater over Phanerozoic time. *Am. J. Sci.* **304**, 438–453.

Bosbach D., Charlet L., Bickmore B. and Hochella M. F. (2000) The dissolution of hectorite: in situ, real-time observations using atomic force microscopy. *Am. Mineral.* **85**, 1209–1216.

Bowser C. J. and Jones B. F. (2002) Mineralogic controls on the composition of natural waters dominated by silicate hydrolysis. *Am. J. Sci.* **302**, 582–662.

Brandt F., Bosbach D., Krawczyk-Barsch E., Arnold T. and Bernhard G. (2003) Chlorite dissolution in the acid pH range: a combined microscopic and macroscopic approach. *Geochim. Cosmochim. Acta* **67**, 1451–1461.

Cama J. and Ganor J. (2006) The effects of organic acids on the dissolution of silicate minerals: a case study of oxalate catalysis of kaolinite dissolution. *Geochim. Cosmochim. Acta* **70**, 2191–2209.

Dove P. M. and Platt F. M. (1996) Compatible real-time rates of mineral dissolution by atomic force microscopy(AFM). *Chem. Geol.* **127**, 331–338.

Drever J. I. and Stillings L. L. (1997) The role of organic acids in mineral weathering. *Colloids Surf. A* **120**, 167–181.

Eggleton R. A. and Banfield J. F. (1985) The alteration of granitic biotite to chlorite. *Am. Mineral.* **70**, 902–910.

Ganor J., Reznik I. J. and Rosenberg Y. O. (2009) Organics in water–rock interactions. *Rev. Mineral. Geochem.* **70**, 259–370.

Golubev S. V., Bauer A. and Pokrovsky O. S. (2006) Effect of pH and organic ligands on the kinetics of smectite dissolution at 25° C. *Geochim. Cosmochim. Acta* **70**, 4436–4451.

Gratz A. J., Hillner P. E. and Hansma P. K. (1993) Step dynamics and spiral growth on calcite. *Geochim. Cosmochim. Acta* **57**, 491–495.

Gratz A. J., Manne S. and Hansma P. K. (1991) Atomic force microscopy of atomic-scale ledges and etch pits formed during dissolution of quartz. *Science* **251**, 1343–1346.

Griffiths R. P., Banham J. E. and Caldwell B. A. (1994) Soil solution chemistry of ectomycorrhizal mats in forest soil. *Soil Biol. Biochem.* **26**, 331–337.

Hajash A. J. (1994) Comparison and evaluation of experimental studies on dissolution of minerals by organic acids. In *Organic Acids in Geological Processes* (eds. E. D. Pittman and M. D. Lewan). Springer-Verlag, Berlin.

Hamer M., Graham R. C., Amrhein C. and Bozhilov K. N. (2003) Dissolution of ripidolite (Mg, Fe-Chlorite) in organic and inorganic acid solutions. *Soil Sci. Soc. Am. J.* **67**, 654–661.

Haward S. J., Shewry P. R., Miles M. J. and McMaster T. J. (2010) Direct real-time imaging of protein adsorption onto hydrophilic and hydrophobic surfaces. *Biopolymers* **93**, 74–84.

Haward S. J., Shewry P. R., Marsh J., Miles M. J. and McMaster T. J. (2011) Force spectroscopy of an elastic peptide: effect of D2O and temperature on persistence length. *Microsc. Res. Tech.* **74**, 170–176.

Hinsinger P. and Jaillard B. (1993) Root-induced release of interlayer potassium and vermiculitization of phlogopite as related to potassium depletion in the rhizosphere of ryegrass. *Eur. J. Soil Sci.* **44**, 525–534.

Jordan G. and Rammensee W. (1996) Dissolution rates and activation energy for dissolution of brucite (0 0 1): a new method based on the microtopography of crystal surfaces. *Geochim. Cosmochim. Acta* **60**, 5055–5062.

Kalinowski B. E. and Schweda P. (1996) Kinetics of muscovite, phlogopite, and biotite dissolution and alteration at pH 1–4, room temperature. *Geochim. Cosmochim. Acta* **60**, 367–385.

Lindgreen H., Garnaes J., Hansen P. L., Besenbacher F., Laesgaard E., Stensgaard I., Gould S. A. C. and Hansma P. K. (1991) Ultrafine particles of North Sea illite/smectite clay minerals investigated by STM and AFM. *Am. Mineral.* **76**, 1218–1222.

Lucas Y. (2001) The role of plants in controlling rates and products of weathering: importance of biological pumping. *Annu. Rev. Earth Planet. Sci.* **29**, 135–163.

Mahlin D., Berggren J., Alderborn G. and Engstrom S. (2004) Moisture-induced surface crystallization of spray-dried amorphous lactose particles studied by atomic force microscopy. *J. Pharm. Sci.* **93**, 29–37.

Malström M. and Banwart S. (1997) Biotite dissolution at 25 C: the pH dependence of dissolution rate and stoichiometry. *Geochim. Cosmochim. Acta* **61**, 2779–2799.

Maurice P. A., McKnight D. M., Leff L., Fulghum J. E. and Gooseff M. (2002) Direct observations of aluminosilicate weathering in the hyporheic zone of an Antarctic Dry Valley stream. *Geochim. Cosmochim. Acta* **66**, 1335–1347.

Metz V. and Ganor J. (2001) Stirring effect on kaolinite dissolution rate. *Geochim. Cosmochim. Acta* **65**, 3475–3490.

Murakami T., Utsunomiya S., Yokoyama T. and Kasama T. (2003) Biotite dissolution processes and mechanisms in the laboratory and in nature: early stage weathering environment and vermiculitization. *Am. Mineral.* **88**, 377–386.

Murphy S. F., Brantley S. L., Blum A. E., White A. F. and Dong H. (1998) Chemical weathering in a tropical watershed, Luquillo Mountains, Puerto Rico: II. Rate and mechanism of biotite weathering. *Geochim. Cosmochim. Acta* **62**, 227–243.

Nesbitt H. W. and Young G. M. (1984) Prediction of some weathering trends of plutonic and volcanic-rocks based on thermodynamic and kinetic considerations. *Geochim. Cosmochim. Acta* **48**, 1523–1534.

Oelkers E. H. and Schott J. (1998) Does organic acid adsorption affect alkali-feldspar dissolution rates? *Chem. Geol.* **151**, 235–245.

Oelkers E. H., Schott J., Gauthier J. M. and Herrero-Roncal T. (2008) An experimental study of the dissolution mechanism and rates of muscovite. *Geochim. Cosmochim. Acta* **72**, 4948–4961.

Rufe E. and Hochella M. F. (1999) Quantitative assessment of reactive surface area of phlogopite during acid dissolution. *Science* **285**, 874–876.

Schnitzer M. and Kodama H. (1976) The dissolution of micas by fulvic acid. *Geoderma* **15**, 381–391.

Stillings L. L., Drever J. I. and Poulson S. R. (1998) Oxalate adsorption at a plagioclase (An47) surface and models for ligand-promoted dissolution. *Environ. Sci. Technol.* **32**, 2856–2864.

Stumm W. and Furrer G. (1987) The dissolution of oxides and aluminium silicates; examples of surface-controlled kinetics. In *Aquatic Surface Chemistry: Chemical Processes at the Particle-Water Interface* (ed. W. Stumm). Wiley, New York.

Stumm W. and Wieland E. (1990) Dissolution of oxide and silicate minerals: rates depend on surface speciation. In *Aquatic Chemical Kinetics: Reacion Rates of Processes in Natural Waters* (ed. W. Stumm). Wiley, New York.

Taylor A. S., Blum J. D., Lasaga A. C. and MacInnis I. N. (2000) Kinetics of dissolution and Sr release during biotite and phlogopite weathering. *Geochim. Cosmochim. Acta* **64**, 1191–1208.

Tu S.-X., Guo Z.-F. and Sun J.-H. (2007) Effect of oxalic acid on potassium release from typical chinese soils and minerals. *Pedosphere* **17**, 457–466.

Turpault M.-P. and Trotignon L. (1994) The dissolution of biotite single crystals in dilute HNO3 at 24 C: evidence of an anisotropic corrosion process of micas in acidic solutions. *Geochim. Cosmochim. Acta* **58**, 2761–2775.

van Hees P. A. W., Lundstrom U. S. and Morth C.-M. (2002) Dissolution of microcline and labradorite in a forest O horizon extract: the effect of naturally occuring organic acids. *Chem. Geol.* **189**, 199–211.

Welch S. A. and Ullman W. J. (1996) Feldspar dissolution in acidic and organic solutions: compositional and pH dependence of dissolution rate. *Geochim. Cosmochim. Acta* **60**, 2939–2948.

White A. F., Blum A. E., Bullen T. D., Davison V. V., Schulz M. and Fitzpatrick J. (1999) The effect of temperature on experimental and natural chemical weathering rates of granitoid rocks. *Geochim. Cosmochim. Acta* **63**, 3277–3291.

Yip C. M. and Ward M. D. (1996) Atomic force microscopy of insulin single crystals: direct visualization of molecules and crystal growth. *Biophys. J.* **71**, 1071–1078.

Associate editor: Jacques Schott